

Plasmoid Ejection by Alfvén Waves and the Fast Radio Bursts from SGR 1935+2154

Yajie Yuan D. Andrei M. Beloborodov A., Alexander Y. Chen D., and Yuri Levin A., S.

1 Center for Computational Astrophysics, Flatiron Institute, 162 Fifth Avenue, New York, NY 10010, USA; yyuan@flatironinstitute.org

2 Physics Department and Columbia Astrophysics Laboratory, Columbia University, 538 West 120th Street, New York, NY 10027, USA; amb@phys.columbia.edu

3 Max Planck Institute for Astrophysics, Karl-Schwarzschild-Str. 1, D-85741 Garching, Germany

4 Department of Astrophysical Sciences, Princeton University, Princeton, NJ 08544, USA

5 Department of Physics and Astronomy, Monash University, Clayton, VIC 3800, Australia

Received 2020 June 5; revised 2020 August 12; accepted 2020 August 15; published 2020 September 4

Abstract

Using numerical simulations we show that low-amplitude Alfvén waves from a magnetar quake propagate to the outer magnetosphere and convert to "plasmoids" (closed magnetic loops) that accelerate from the star, driving blast waves into the magnetar wind. Quickly after its formation, the plasmoid becomes a thin relativistic pancake. It pushes out the magnetospheric field lines, and they gradually reconnect behind the pancake, generating a variable wind far stronger than the normal spindown wind of the magnetar. Repeating ejections drive blast waves in the amplified wind. We suggest that these ejections generate the simultaneous X-ray and radio bursts detected from SGR 1935+2154. A modest energy budget of the magnetospheric perturbation $\sim 10^{40}$ erg is sufficient to produce the observed bursts. Our simulation predicts a narrow (a few milliseconds) X-ray spike from the magnetosphere, arriving almost simultaneously with the radio burst emitted far outside the magnetosphere. This timing is caused by the extreme relativistic motion of the ejecta.

Unified Astronomy Thesaurus concepts: Magnetars (992); Neutron stars (1108); Non-thermal radiation sources (1119); Radio transient sources (2008); Shocks (2086); Radio bursts (1339)

1. Introduction

Neutron stars with ultrastrong magnetic fields $B \sim 10^{14}$ – 10^{16} G (dubbed "magnetars" by Duncan & Thompson 1992) exhibit extreme X-ray activity (see Kaspi & Beloborodov 2017 for a review). Magnetars were also suspected as sources of fast radio bursts (FRBs), and the detection of FRBs from SGR 1935+2154 on 2020 April 28 has established this connection (Bochenek et al. 2020; The CHIME/FRB Collaboration et al. 2020). SGR 1935+2154 is a magnetar residing in our galaxy. It has spin period $P \approx 3.2$ s and magnetic dipole moment $\mu \sim 2 \times 10^{32}$ G cm³, which corresponds to a surface magnetic field $B_{\star} \sim 2 \times 10^{14}$ G.

Scenarios for FRB emission by magnetars can now be put to test. One mechanism is an ultrarelativistic ejection, which launches a blast wave far beyond the magnetosphere (Lyubarsky 2014; Beloborodov 2017, 2020, hereafter B17, B20). This model invokes synchrotron maser emission by the collisionless shock from the explosion. The shock can propagate in the magnetar wind of relativistic e^{\pm} pairs or in a slow baryonic outflow (B17, B20; Metzger et al. 2019; Margalit et al. 2020b). It has also been proposed that FRBs can come directly from the neutron star magnetosphere (Lyutikov 2002; Katz 2016; Kumar et al. 2017; Lu et al. 2020; Lyutikov & Popov 2020). In this scenario, a concrete mechanism for coherent emission is yet to be worked out.

The most common form of magnetar activity is the hard X-ray bursts with energies $\mathcal{E}_X \sim 10^{39} \text{--}10^{41}$ erg. This nonthermal activity must be generated by surface motions of the neutron star, which can both slowly twist the magnetosphere and quickly launch Alfvén waves (Blaes et al. 1989; Thompson & Duncan 1996). Intriguingly, the two radio bursts of millisecond duration detected from SGR 1935+2154 observed during an X-ray burst, which lasted ~ 0.5 s and had an energy of $\sim 10^{40}$ erg, assuming a distance of ~ 10 kpc (Li et al. 2020; Mereghetti et al. 2020; Ridnaia et al. 2020). Each FRB arrived a few milliseconds ahead of a narrow X-ray spike of energy

 $\mathcal{E}_X \lesssim 10^{39}$ erg, exceeding the FRB energy by a factor $> 10^3$. The energy budget of magnetospheric perturbations generating this activity is likely a few times 10^{40} erg, depending on the efficiency and beaming of the X-ray emission. This energy is only $\sim 10^{-6}$ of the total magnetospheric energy.

A question arises whether such low-energy events should produce ejecta from the magnetosphere, which is essential for the blast-wave FRB mechanism. In this Letter we investigate the magnetospheric response to a small shear perturbation of the magnetar surface. We calculate the magnetospheric dynamics in the framework of force-free electrodynamics (FFE), similar to Parfrey et al. (2013). We use our own finite difference code COmputational Force FreE Electrodynamics ($Coffee^6$; Chen et al. 2020). The numerical method is described elsewhere (Yuan et al. 2020). The simulation assumes efficient e^{\pm} creation to maintain the FFE approximation at low energy costs. This assumption is likely satisfied by magnetars (B20).

2. Alfvén Waves from Starquakes

Sudden excitations of crustal shear oscillations (starquakes) were invoked to explain X-ray bursts from magnetars (Thompson & Duncan 1996). Their energy could reach $E_Q^{\rm max} \sim V \mu_{\rm sh} s^2/2 \sim 10^{44} \, V_{16} (s/0.1)^2$ erg, where $\mu_{\rm sh} \sim 10^{30}$ erg cm⁻³ is the shear modulus of the deep crust, s < 0.1 is the elastic strain, and V is the stressed volume (a fraction of the deep crust volume $\sim 10^{17} \, {\rm cm}^3$).

⁶ https://github.com/fizban007/CoffeeGPU

⁷ Quakes likely involve new forms of crustal response to magnetic stresses, which remain to be understood. Beloborodov & Levin (2014) showed that thermoplastic instabilities develop in the stressed crust, in particular when the ultrastrong *B* suppresses normal yielding (Levin & Lyutikov 2012). Thompson et al. (2017) argued that the crustal yielding can develop quickly, on a millisecond timescale.

After its trigger stops, the quake duration t_Q is limited by the magnetic coupling of the crust to the liquid core (Levin 2006; Bransgrove et al. 2020). The coefficient of shear wave transmission to the core $\mathcal{T}_c \sim 0.1 B_{14}^{1/2}$ is controlled by the poloidal magnetic field B. The waves will bounce at least $\sim \mathcal{T}_c^{-1}$ times, spreading through the crust. They propagate with speed $\sim 10^8$ cm s⁻¹, and each quake should last tens of milliseconds, with wave frequencies $\nu \gtrsim 1$ kHz. A series of quakes can make the activity much longer.

The quake launches Alfvén waves into the magnetosphere (Blaes et al. 1989; Thompson & Duncan 1996; Bransgrove et al. 2020). Waves are launched on the magnetospheric field lines whose length exceeds the wavelength $\lambda = c/\nu \approx 3 \times 10^7 \, \nu_{\rm kHz}^{-1}$ cm, which is much greater than the star's radius $R_{\star} \approx 10^6\,$ cm.

Far from the star, the magnetic field lines are approximately dipole and reach their maximum radii R at the magnetic equator. A field line extending to radius $R \gg R_{\star}$ has the approximate length $\sim 3R$. Thus, the waves are launched on field lines extending to

$$R > 10^7 \,\nu_{\rm kHz}^{-1} \,\rm cm.$$
 (1)

The magnetic flux reaching the sphere of radius R is $\Psi = 2\pi\mu/R$ (where μ is the magnetic dipole moment). The footprint area of flux Ψ on the star's surface is $A \sim \Psi/B_{\star}$, where B_{\star} is the surface magnetic field. In particular, for an approximately dipole magnetosphere, $\mu \sim B_{\star}R_{\star}^3$ and $A \sim 2\pi R_{\star}^3/R$.

The Alfvén waves emitted along the extended field lines over the quake duration t_Q carry a small fraction f of the quake energy (Bransgrove et al. 2020), with power

$$L_{\rm A} \sim 10^{42} \left(\frac{f}{0.01}\right) \left(\frac{E_Q}{10^{42} \,{\rm erg}}\right) \left(\frac{t_Q}{10 \,{\rm ms}}\right)^{-1} \frac{{\rm erg}}{{\rm s}}.$$
 (2)

The relative amplitude of the wave $\delta B/B$ is small near the star, $\delta B_{\star}/B_{\star} \ll 1$, and grows with radius r,

$$\frac{\delta B}{B} = \frac{\delta B_{\star}}{B_{\star}} \left(\frac{r}{R_{\star}}\right)^{3/2}.$$
 (3)

3. Plasmoid Ejection

The wave growth with r leads to $\delta B > B$ on sufficiently extended field lines, $R/R_{\star} > (\delta B_{\star}/B_{\star})^{-2/3}$. Then, as demonstrated below, the wave generates a closed magnetic island ("plasmoid") and ejects it from the magnetosphere. This occurs far from the star, where the magnetospheric energy $\sim R^3 B^2$ is comparable to the wave energy $\mathcal{E}_{\rm w}$. The ejecta energy is

$$\mathcal{E}_p \sim \mathcal{E}_w \sim R^3 B^2 \sim \frac{\mu^2}{R^3} = 10^{40} \,\mu_{32}^2 \,R_8^{-3} \,\text{erg}.$$
 (4)

Our simulation is axisymmetric and starts with a steady-state, force-free dipolar magnetosphere attached to a rotating star (with aligned magnetic and rotational axes). At t=0, a sinusoidal Alfvén wave is injected by shearing the footprints of the closed magnetic field lines that extend to $R \sim 10^8$ cm. We injected a packet of four wavelengths $\lambda = 2.5 \times 10^7$ cm to demonstrate one plasmoid formation, and then (30 ms later) another packet, to illustrate multiple plasmoid ejections. The energy of each packet is $\mathcal{E}_w \approx 9 \times 10^{40}$ erg. The initial wave amplitude is small, $\delta B_\star/B_\star \approx 0.004$, and its propagation for a

while follows Equation (3).⁸ Interesting nonlinear evolution occurs at $r \sim 10^8$ cm where δB exceeds B (Figure 1).

We observe that at the radius $R_{\rm ej} \approx 10^8\,{\rm cm}$ the Alfvén wave "breaks" and forms a plasmoid with energy $\mathcal{E}_p \sim 0.6\,\mathcal{E}_w$. The plasmoid immediately accelerates away, pushing its way through the outer magnetosphere. The ambient magnetic energy decreases with radius as $r^3B^2 \propto r^{-3}$ and quickly becomes negligible compared with \mathcal{E}_p , so the plasmoid continues to expand freely, unaffected by the background. Its transverse size scales linearly with r while its radial thickness remains approximately constant, $\Delta \sim 10^8\,{\rm cm}$, so the plasmoid becomes a thin pancake. Its Lorentz factor quickly grows to $\gamma > 10^2$ (Figure 2). The pancake occupies an extended solid angle around the magnetic equator. Most of its energy is contained in an angular range $\Delta\theta \sim 0.4$.

The pancake structure reflects the initial shape of the Alfvén wave at $r \ll R_{\rm ej}$ and the process of its breakout at $R_{\rm ej}$. The Alfvén wave carries the perturbations B_ϕ and E_θ , which are supported by an electric current J along the background dipole magnetic field. As the wave packet breaks away, these field components and the current are advected with the plasmoid. In addition, a strong electromagnetic wave of E_ϕ and δB_θ (with J=0) is launched ahead of the current-carrying plasmoid.

This ejecta forces the magnetosphere to open up, creating a Y-shaped current sheet separating the opposite magnetic fluxes in the two hemispheres (Figure 3). The current sheet is unstable to reconnection, and the opposite magnetic fluxes combed out by the pancake gradually snap back behind it, ejecting numerous small-scale plasmoids of various sizes and energies. A similar plasmoid chain formed in the flare simulations of Parfrey et al. (2013). The equatorial current sheet extends to the southern end of the pancake; reconnection also occurs there (Figure 3).

Reconnection at the ejection site continues to generate a variable outflow until the second Alfvén wave packet arrives at $R_{\rm ej}$, and then the second pancake is ejected (Figures 1–2). The entire region between the two pancakes is filled with the variable wind generated by magnetic reconnection. This wind forms the ambient medium encountered by the second pancake. The wind power $L_{\rm w}(t)$ is much lower than the pancake power $\sim \mathcal{E}_p c/R_{\rm ej} \sim L_{\rm A}$ and much greater than the spindown power of the magnetar $L_0 \approx \mu^2 \Omega^4/c^3$ (Figure 4).

After crossing the light cylinder $R_{LC} = c/\Omega$, the leading pancake begins to sweep the toroidal spindown wind of the magnetar. The second pancake continues to sweep the variable flow between the two pancakes.

In our simulation, the light cylinder is located at $R_{\rm LC} = 1.5 \times 10^9$ cm, which is 10 times smaller than $R_{\rm LC}$ in SGR 1935+2154, i.e., our star rotates 10 times faster. This choice was made to accommodate $R_{\rm LC}$ in the computational domain well inside of its outer boundary $R_{\rm out} = 5 \times 10^9$ cm. However, the pancakes and the wind between them formed at $r \ll R_{\rm LC}$ unaffected by the magnetar rotation, so their parameters need no rescaling.

The simulation shows that about 60% of the initially injected wave energy is carried away by the ejecta, and 10%–20% is

 $[\]overline{^8}$ Our simulation verified the law $\delta B/B = (\delta B_{\star}/B_{\star})(r/R_{\star})^{3/2}$ during the linear phase $\delta B \ll B$, and then we removed the trivial linear evolution phase by moving the inner boundary of the simulation box from R_{\star} to $R_{\rm inj} \approx 10 R_{\star}$ while correspondingly increasing the injected amplitude by $(R_{\rm inj}/R_{\star})^{3/2} \approx 32$, from $\delta B_{\star}/B_{\star} \approx 0.004$ at R_{\star} to $\delta B/B \approx 0.13$ at $R_{\rm inj}$.

⁹ The simulation is axisymmetric and performed in spherical coordinates r, θ , ϕ . We use a 8192×4096 grid with uniform spacing in $\ln r$ and θ , covering the region $10^7 < r < 5 \times 10^9$ cm.

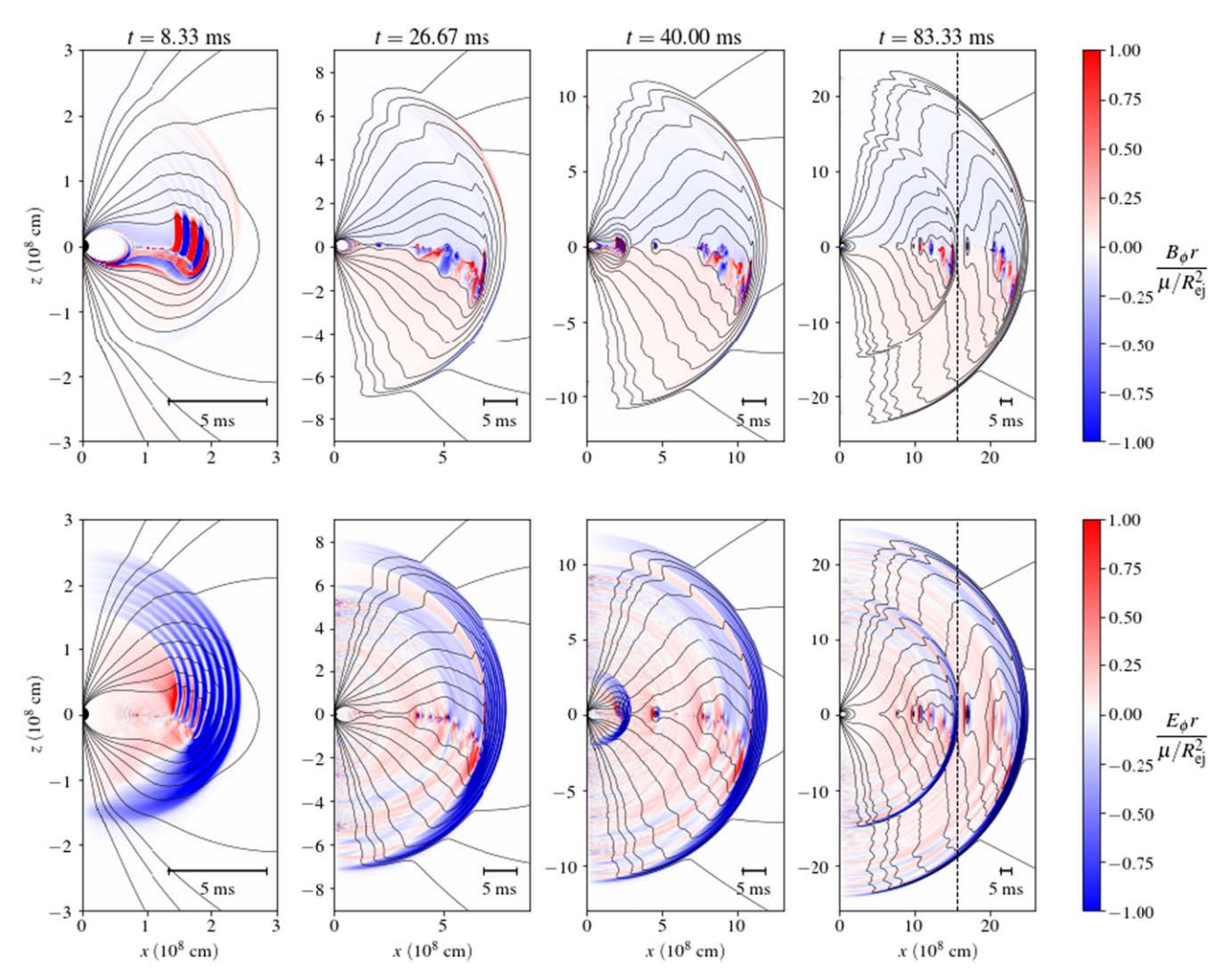


Figure 1. Four snapshots of the simulation. Thin black curves are the poloidal magnetic field lines. Color shows rB_{ϕ} (top) and rE_{ϕ} (bottom). Lengths are normalized to the ejection radius $R_{\rm ej} = 10^8$ cm, and fields are normalized to $B_0 = \mu/R_{\rm ej}^3$, where μ is the magnetic dipole moment of the star. The vertical dashed line indicates the light cylinder $R_{\rm LC} = c/\Omega$.

dissipated. The dissipation occurs in the current sheets that form during the ejection process (Figure 3). It is captured only approximately in FFE simulations, via three numerical channels. (1) To satisfy the FFE conditions, at every time step we remove any $E \cdot B$ by resetting $E \rightarrow E - (E \cdot B)B/B^2$. (2) Whenever E > B happens, we reset E to (B/E) E. (3) We apply the standard suppression of high frequency noise (Kreiss & Oliger 1973). The resulting numerical dissipation occurs mainly in the thin current sheets, and serves as a proxy of physical dissipation.

Assuming that the dissipated energy is emitted isotropically in the local plasma rest frame, we have calculated the bolometric light curve of this emission (Figure 5). The plasma moves with velocity $\mathbf{v} = \mathbf{E} \times \mathbf{B}/B^2$, and part of the dissipation occurs where the ejecta have already accelerated, which leads to strong Doppler boosting. In particular, substantial emission comes from the current sheet at the southern tail of the pancake, which develops a high Lorentz factor γ (Figure 3), and there is a similar current sheet in the second pancake. This results in the two strong spikes in the light curve. ¹⁰ A significant part of

this emission should appear in the X-ray band, and thus two X-ray spikes are predicted by the simulation. The centroid of the X-ray spike is delayed by a few milliseconds relative to the blast-wave emission (Figure 5).

4. FRB Emission from the Explosion

4.1. Shock Maser Emission

An observer at polar angle θ will see the pancake with the apparent energy

$$\mathcal{E}(\theta) = 4\pi \frac{d\mathcal{E}_p}{d\Omega} = b(\theta)\mathcal{E}_p. \tag{5}$$

In our simulation, the beaming factor $b(\theta)$ is found to vary from $b \ll 1$ to $b \sim 5$ for favorable lines of sight. The isotropic equivalent of the explosion power $L_{\rm f}(\theta)$ is related to the original Afvén wave power $L_{\rm A}$ as

$$L_{\rm f}(\theta) \sim b(\theta) L_{\rm A}.$$
 (6)

It will drive an ultrarelativistic blast wave in the wind.

Calculations of maser radio emission from the blast wave are based on kinetic simulations of collisionless shocks (e.g., Plotnikov & Sironi 2019) and give the following (see B20). If

 $[\]overline{^{10}}$ Figure 5 includes dissipation at $r < 6R_{\rm ej}$, as the declining resolution $\delta r \propto r$ complicates dissipation measurements at $r \gtrsim 10R_{\rm ej}$. Including $r > 6R_{\rm ej}$ would make the two spikes higher.

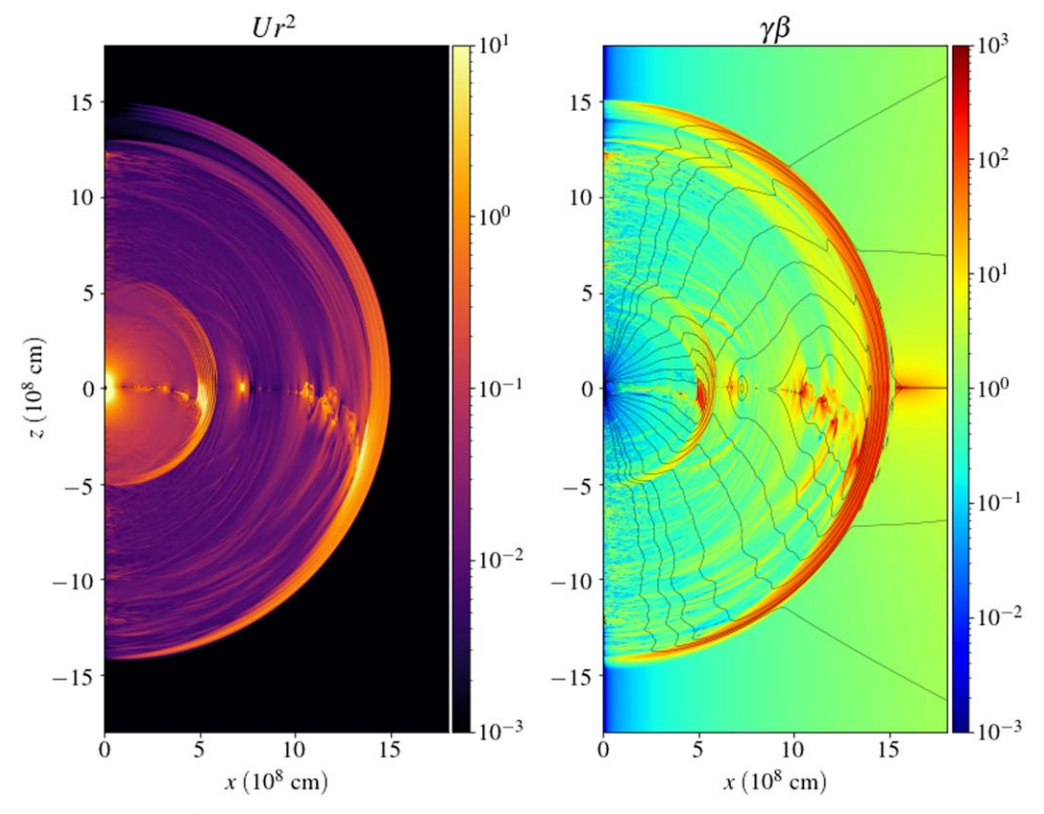


Figure 2. Left: energy density $U = (B^2 + E^2)/8\pi$. Right: $E \times B$ drift 4-velocity. The snapshot is taken at t = 50 ms. Units are the same as in Figure 1.

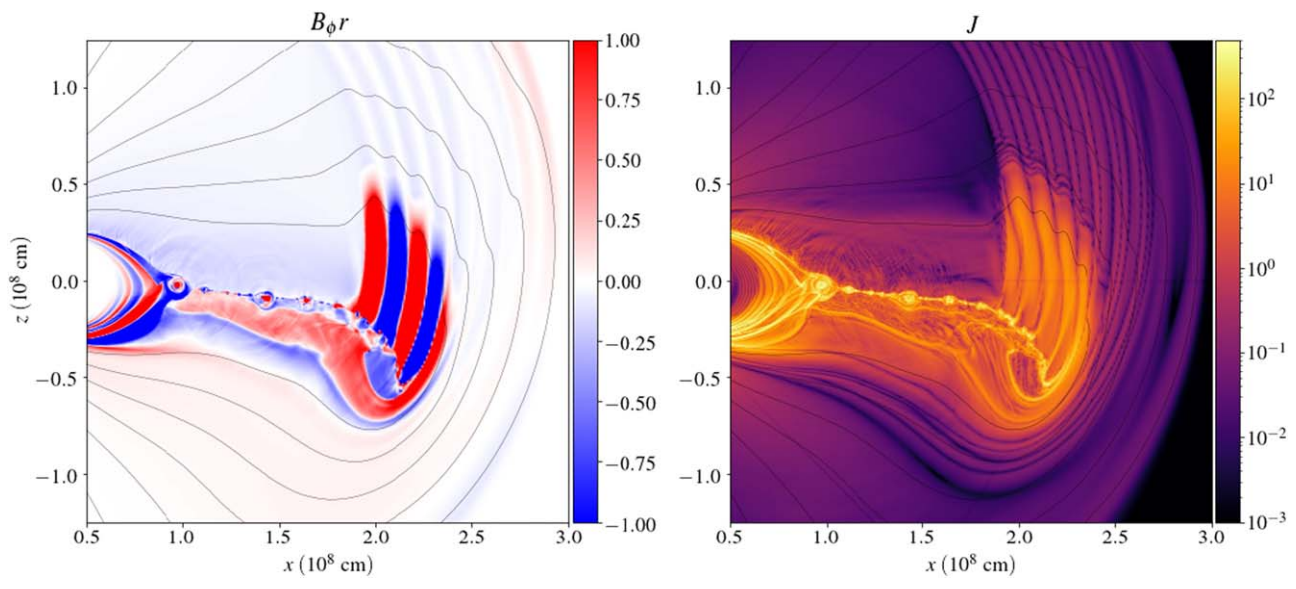


Figure 3. Zoom-in view of the ejecta at t = 10 ms. Left: toroidal field B_{ϕ} . Right: magnitude of current J. Units are the same as in Figure 1.

the GHz waves are emitted before the blast wave begins to decelerate, the radio burst has the apparent energy

$$\mathcal{E}_{\text{FRB}} \sim 10^{-3} L_{\text{f}} \delta t_{\text{obs}} \sim 10^{36} L_{\text{f,42}} \left(\frac{\delta t_{\text{obs}}}{1 \text{ ms}} \right) \text{erg.}$$
 (7)

The burst duration $\delta t_{\rm obs}$ is

$$\delta t_{\rm obs} \sim \frac{r}{c\Gamma_{\rm sh}^2}, \qquad \Gamma_{\rm sh} = 2\sigma_{\rm w}^{1/2}\Gamma_{\rm w} \left(\frac{L_{\rm f}}{L_{\rm w}}\right)^{1/4}.$$
 (8)

Here $\Gamma_{\rm sh}$ is the shock Lorentz factor; $L_{\rm w}$, $\sigma_{\rm w}$, $\Gamma_{\rm w}$ are the power, magnetization parameter, Lorentz factor of the upstream wind swept by the shock.

Consider the wind behind pancake 1. It serves as the external medium for pancake 2 (Figure 2). The wind power and speed profiles grow outward, reaching maximum at pancake 1. The blast wave from pancake 2 will chase the wind layers, so that at radius r it picks up layers with $\Gamma_{\rm w}^2 \sim r/cT$, where $T \sim 30\,{\rm ms}$ is the time separating the two

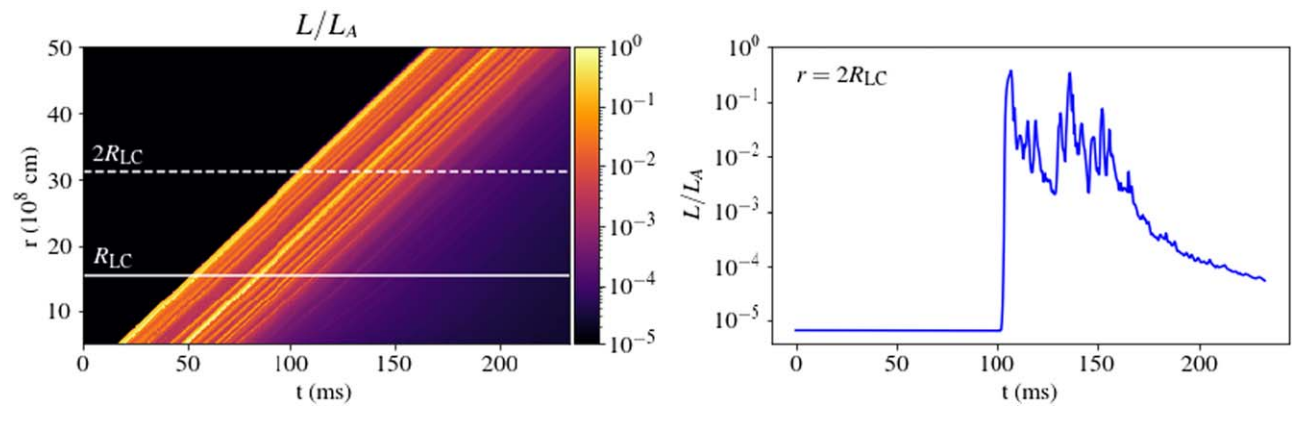


Figure 4. Left: net Poynting flux L(t, r) (through spheres of different radii r) normalized to the Alfvén wave luminosity L_A . Right: L(t) at $r = 2R_{LC}$ (along the dashed line in the left panel).

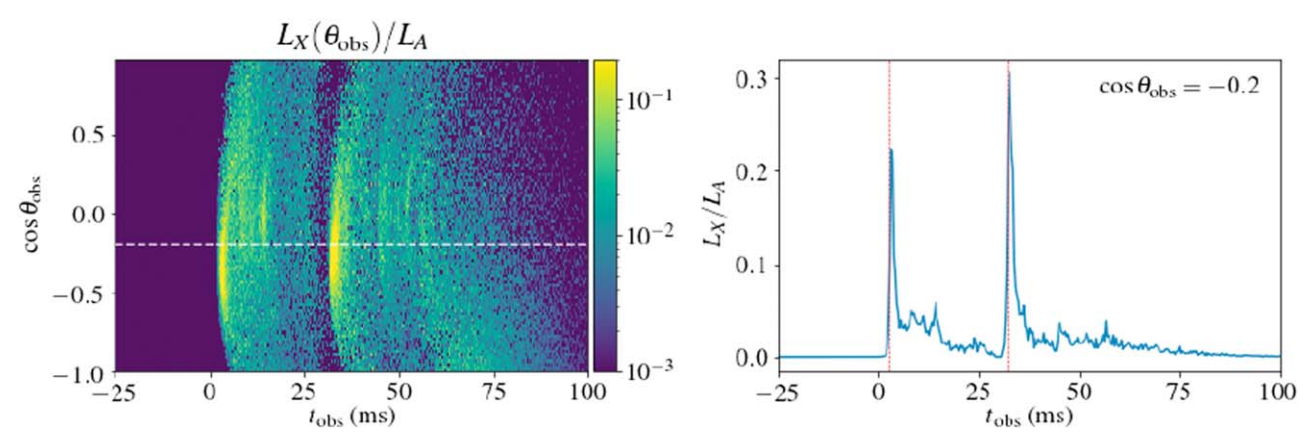


Figure 5. Left: distribution of apparent X-ray luminosity $L_{\rm X}(\theta_{\rm obs})$ over polar directions $\theta_{\rm obs}$ and arrival times $t_{\rm obs}$. Right: X-ray light curve seen by an observer at $\cos\theta_{\rm obs}=-0.2$ (white dashed line in the left panel). The vertical red dashed lines mark the arrival times of the blast-wave emission at $r\gtrsim 10^{13}$ cm.

pancakes. This gives

$$\delta t_{\rm obs} \sim \frac{T}{4\sigma_{\rm w}} \left(\frac{L_{\rm w}}{L_{\rm f}}\right)^{1/2} \sim \frac{1 \text{ ms}}{\sigma_{\rm w}} \left(\frac{T}{30 \text{ ms}}\right) \left(\frac{L_{\rm w,40}}{L_{\rm f,42}}\right)^{1/2}.$$
 (9)

The shock emits in the GHz band at radius

$$R_{\rm GHz} \sim 10^{13} L_{\rm f,42}^{1/4} L_{\rm w,40}^{1/4} \, {\rm cm}.$$
 (10)

 $L_{\rm f}$ depends on the viewing angle θ and decreases outside favorable θ . For instance, $L_{\rm f}\sim 10^{41}~{\rm erg~s^{-1}}$ gives $\mathcal{E}_{\rm FRB}\sim 10^{35}~{\rm erg}$ and $\delta t_{\rm obs}\sim 3\sigma_{\rm w}^{-1}~{\rm ms}$, suitable for the FRBs from SGR 1935+2154.

Multiple ejections can result in multiple blast waves in the enhanced wind, and thus produce multiple FRBs. The small $\delta t_{\rm obs}$ implies that their arrival times closely track the pancake ejection time, and so the FRBs arrive simultaneously with the X-rays generated by the ejections (Figure 5).

4.2. Magnetosonic Waves Carried by the Pancake

In our simulation we observed formation of current sheets and waves of various scales during the pancake ejection. High-frequency fluctuations are expected from magnetic reconnection in the current sheets: reconnection forms a self-similar plasmoid chain extending to a microscopic kinetic scale comparable to the particle Larmor radius r_L (e.g., Uzdensky et al. 2010). The chain

is observed in both kinetic (Sironi & Spitkovsky 2014) and FFE (Parfrey et al. 2013) simulations. FFE simulations truncate the chain on the grid scale as they do not follow kinetic processes.

Small-scale plasmoid mergers in the chain generate fast magnetosonic waves with frequencies up to $\nu \sim c/r_{\rm L}$ and energy flux $F \lesssim 10^{-4}cB^2/4\pi$, where B is the reconnecting field (Lyubarsky 2019; Philippov et al. 2019). The high-frequency waves can carry up to 10^{-4} of the energy released by reconnection, comparable to $10^{-4}\mathcal{E}_p$. The pancake ejection in our simulation occurs at radii $r < 10^9\,\mathrm{cm}$ where $B > 10^7\,\mathrm{G}$. The corresponding $r_{\rm L}$ implies that reconnection generates GHz waves, although our simulation can only resolve waves from much larger plasmoids (Figure 1).

In FFE, fast magnetosonic modes are indistinguishable from vacuum electromagnetic waves. In reality, the generated waves live in the plasma of a finite inertia; they are advected with the pancakes. At large radii (far outside the magnetosphere) the waves may escape as radio waves (Lyubarsky 2020) if they are not damped before reaching the escape radius. If only waves carried by the ultrarelativistic pancakes survive, the radio bursts would have durations comparable to the pancake thickness $\Delta/c \sim 3$ ms. This would be consistent with FRBs from SGR 1935-2154.

5. Discussion

Our results demonstrate that flares can occur in the outer magnetosphere and eject plasmoids similarly to the rare, extremely energetic ("giant") flares in the inner magnetosphere. The outer magnetosphere is overtwisted by the outgoing and growing Alfvén wave (while simulations of giant flares invoked quasi-static twisting; e.g., Parfrey et al. 2013; Carrasco et al. 2019). The resulting explosion power $L_{\rm f}$ is comparable to the power of the Alfvén wave launched by the quake, $L_{\rm A}$. Plasmoid ejection by field lines extending to a given radius R has an energy threshold $\mathcal{E}_{\rm thr} \sim \mu^2/R^3 = 10^{40} \, \mu_{32}^2 \, R_8^{-3}$ erg. During the quake activity of a magnetar, the ejections may occur intermittently, depending on the amplitude and location of the quake trigger.

We conclude that a broad range of magnetic ejections with $L_{\rm f}\sim 10^{41}\text{--}10^{47}\,{\rm erg~s^{-1}}$ can occur in magnetars. The picture of blast waves from magnetic flares (B17, B20) then implies a broad range of FRB energies scaling with $L_{\rm f}$ (Equation (7)) and produced by the same mechanism. It includes the repeating superstrong FRBs from young, hyperactive magnetars in distant galaxies and the weak bursts from the local, older magnetar SGR 1935+2154.

Our simulation shows a huge enhancement of the magnetar wind, $L_{\rm w} > 10^{-3} L_{\rm A} \gg L_{\rm sd}$, during the bursting period. Hence, blast waves can propagate in winds much denser than the normal spindown wind. The first blast wave, from pancake 1, may not produce a bright FRB because the wind ahead of it is weak, but the strong wind in the wake of pancake 1 leads to efficient FRB production by the blast wave from pancake 2. The wind is variable and modulates the temporal and spectral structure of the shock maser emission (see Section 6.6 in B20). If the pancake tails are indeed the sites of radio emission, three close ejections may be needed to produce two FRBs detected in SGR 1935+2154. Such conditions, along with a favorable line of sight, are rare. This may explain why only a small fraction of magnetar X-ray bursts are accompanied by FRBs.

Current sheets formed in the wave breakout process are sources of magnetosonic waves, which likely extend to GHz frequencies. Similar waves from magnetic flares are discussed by Most & Philippov (2020) in the context of binary pulsars. If these waves are not damped during subsequent expansion to a much larger radius where they could escape as radio waves, they could provide another source of radio emission. Then more frequent FRBs may be expected from magnetars, as such waves likely accompany every pancake ejection.

Another interesting result of our simulation is the X-ray spike simultaneous with the blast-wave emission. The spike originated from dissipation during the plasmoid ejection, which took place around the magnetic equator and triggered magnetic reconnection. We anticipate that the Alfvén-wave-driven flares can eject plasmoids at different polar angles, with different dissipation rates, and we do not expect a universal energy ratio of the radio and X-ray spikes, $\mathcal{E}_{\rm radio}/\mathcal{E}_{\rm X}$.

Our simulation is just one example illustrating magnetic flares in the outer magnetosphere, which was not fine-tuned to a specific observation. In particular, our flare energy was probably somewhat higher than needed for the 2020 April 28 event in SGR 1935+2154, depending on the viewing angle. Magnetar flares are diverse in energy, and their details should

depend on the initial shape and location of Alfvén wave emission. We leave their systematic study to future work.

Future work can advance the model in a few ways. (1) While our FFE simulations reliably demonstrate the formation of dissipative current sheets, accurate calculations of dissipation will require kinetic modeling. (2) Our axisymmetric simulation shows reconnection of poloidal magnetic field lines, and tracing reconnection of B_{ϕ} will require full 3D simulations. (3) 3D simulations could model non-axisymmetric Alfvén waves and ejecta interacting with striped winds of inclined rotators. Lyubarsky (2020) proposed that this interaction could generate FRBs with frequency $\nu_{\rm FRB} \propto L_{\rm f}^{5/8}$. When applied to explosions in SGR 1935+2154, it gives $\nu_{\rm FRB} \lesssim 1\,$ MHz; however, his model is potentially viable for brighter FRBs.

The possibility of blast waves from SGR 1935+2154 is also discussed by Margalit et al. (2020a), without specifying the mechanism of the low-energy explosion. They consider a blast wave hitting a slowly expanding baryonic cloud at $r \sim 10^{11}$ cm, and find that it would generate radio and X-ray emission with $\mathcal{E}_{\rm radio}/\mathcal{E}_{\rm X} \sim 10^{-5}$.

We thank the referee for helpful comments on the manuscript. Y.Y. is supported by a Flatiron Research Fellowship at the Flatiron Institute, Simons Foundation. A.M.B. is supported by NASA grant NNX 17AK37G, NSF grant AST 2009453, Simons Foundation grant #446228, and the Humboldt Foundation. A.C. is supported by NASA grant 80NSSC18K1099. Y.L. is supported by NSF grant AST 2009453.

ORCID iDs

Yajie Yuan https://orcid.org/0000-0002-0108-4774 Alexander Y. Chen https://orcid.org/0000-0002-4738-1168

References

Beloborodov, A. M. 2017, ApJL, 843, L26

```
Beloborodov, A. M. 2020, ApJ, 896, 142
Beloborodov, A. M., & Levin, Y. 2014, ApJL, 794, L24
Blaes, O., Blandford, R., Goldreich, P., & Madau, P. 1989, ApJ, 343,
Bochenek, C. D., Ravi, V., Belov, K. V., et al. 2020, arXiv:2005.10828
Bransgrove, A., Beloborodov, A. M., & Levin, Y. 2020, ApJ, 897, 173
Carrasco, F., Viganò, D., Palenzuela, C., & Pons, J. A. 2019, MNRAS,
Chen, A. Y., Yuan, Y., & Vasilopoulos, G. 2020, ApJL, 893, L38
Duncan, R. C., & Thompson, C. 1992, ApJL, 392, L9
Kaspi, V. M., & Beloborodov, A. M. 2017, ARA&A, 55, 261
Katz, J. I. 2016, ApJ, 826, 226
Kreiss, H. O., & Oliger, J. 1973, Methods for the Approximate Solution of
  Time Dependent Problems, GARP Publications Series No. 10 (Geneva:
  Global Atmospheric Research Programme—WMO-ICSU Joint Organizing
  Committee)
Kumar, P., Lu, W., & Bhattacharya, M. 2017, MNRAS, 468, 2726
Levin, Y. 2006, MNRAS, 368, L35
Levin, Y., & Lyutikov, M. 2012, MNRAS, 427, 1574
Li, C. K., Lin, L., Xiong, S. L., et al. 2020, arXiv:2005.11071
Lu, W., Kumar, P., & Zhang, B. 2020, arXiv:2005.06736
Lyubarsky, Y. 2014, MNRAS, 442, L9
Lyubarsky, Y. 2019, MNRAS, 483, 1731
Lyubarsky, Y. 2020, ApJ, 897, 1
Lyutikov, M. 2002, ApJL, 580, L65
Lyutikov, M., & Popov, S. 2020, arXiv:2005.05093
Margalit, B., Beniamini, P., Sridhar, N., & Metzger, B. D. 2020a, ApJL,
  899, L27
Margalit, B., Metzger, B. D., & Sironi, L. 2020b, MNRAS, 494, 4627
Mereghetti, S., Savchenko, V., Ferrigno, C., et al. 2020, ApJL, 898, L29
Metzger, B. D., Margalit, B., & Sironi, L. 2019, MNRAS, 485, 4091
```

```
Most, E. R., & Philippov, A. A. 2020, ApJL, 893, L6
Parfrey, K., Beloborodov, A. M., & Hui, L. 2013, ApJ, 774, 92
Philippov, A., Uzdensky, D. A., Spitkovsky, A., & Cerutti, B. 2019, ApJL, 876, L6
Plotnikov, I., & Sironi, L. 2019, MNRAS, 485, 3816
Ridnaia, A., Svinkin, D., Frederiks, D., et al. 2020, arXiv:2005.11178
Sironi, L., & Spitkovsky, A. 2014, ApJL, 783, L21
```

```
The CHIME/FRB Collaboration, Andersen, B. C., et al. 2020, arXiv:2005. 10324

Thompson, C., & Duncan, R. C. 1996, ApJ, 473, 322

Thompson, C., Yang, H., & Ortiz, N. 2017, ApJ, 841, 54

Uzdensky, D. A., Loureiro, N. F., & Schekochihin, A. A. 2010, PhRvL, 105, 235002

Yuan, Y., Levin, Y., Bransgrove, A., & Philippov, A. 2020, arXiv:2007.11504
```